

Seismic tomography of a Maya pyramid: Chan Chich, Belize

Chuangdong Xu and Robert R. Stewart

ABSTRACT

A seismic survey was conducted on a Mayan pyramid ruin at Chan Chich, Belize, Central America in June, 2000. The purpose of this survey was to test whether a hammer seismic technique could propagate energy through the carbonate-rubble and mortar pyramid (30 m x 30 m at the base), and if this energy could be used to make images of the interior of the structure. To this end, ten 3-component geophones were planted, with 2 m spacing, on one side of the pyramid. Source points were acquired around the corner on an adjacent side of the pyramid at a 4 m spacing – giving a geometry like that of a VSP on its side. The sledge-hammer source was struck about 20 times per shot point. We analyze the VSP-type dataset here by picking first-break arrivals from 60 seismic traces and performing a travelttime inversion to estimate the velocities inside the pyramid. Finally, a velocity contour map is given with resolution and reliability analysis. We find that the near-surface of the pyramid has velocities about 100~200 m/s while the interior has higher velocities (500 m/s to 700 m/s). There is evidence of a low velocity region amongst the higher velocity areas.

INTRODUCTION

In June 2000, a seismic survey on a Maya pyramid ruin was acquired in Belize, Central America at the Chan Chich archeological site. The carbonate rubble and mortar pyramid has rounded corners and a soft-soil surface covered by tropical jungle. The pyramid is about 30 m by 30 m at the base and stands some 18 m high. A unique seismic dataset was acquired: five hammer-seismic sources were located on one side of the pyramid, juxtaposed with ten 3-component geophones planted on the adjacent, perpendicular side. The 3-C receivers were spaced along a 2 m contour level, up from the base of the pyramid, and at a 2 m horizontal spacing. The shots were spaced a nominal 4 m on the perpendicular side. One shot (#6) is on the same side of the pyramid as the receivers, between receiver #1 and #2. This survey geometry is thus like a VSP on its side (Figure 1).

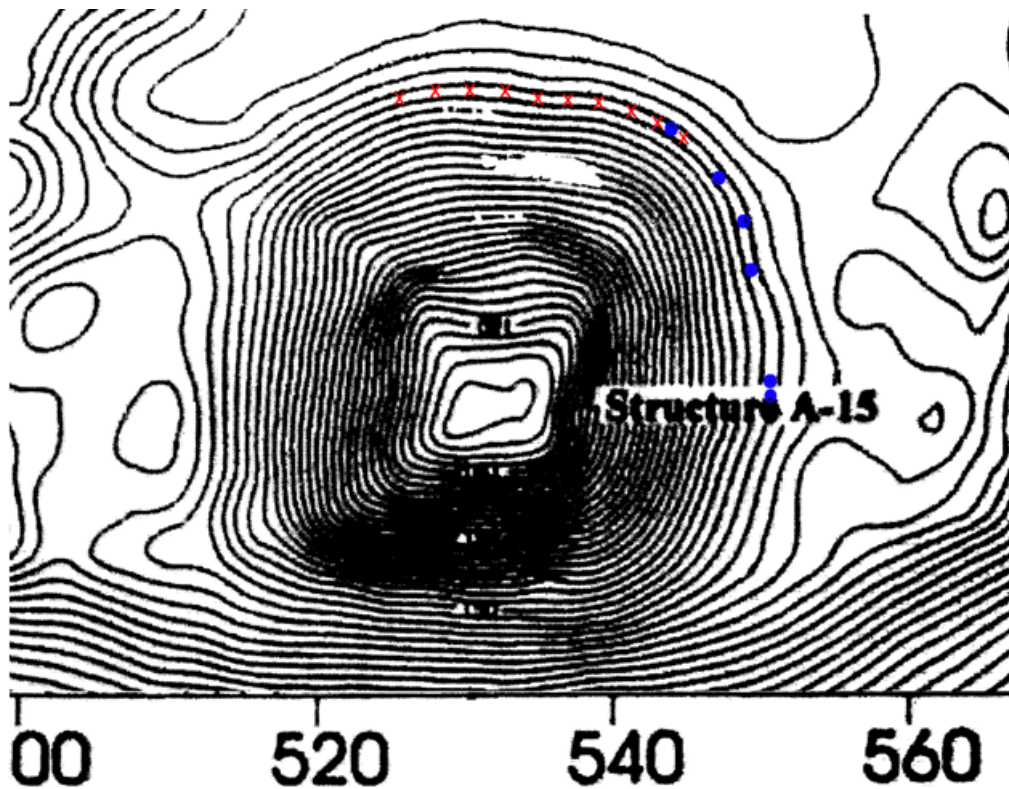


Figure 1. Topographic contour map of the pyramid. The pyramid is about 30 m by 30 m at its base. Annotations are in meters. The survey geometry is overlain with blue dots indicating shots and red "x"s denoting geophone location.

Sixty first-arrival time picks are made using the 6 shots and 10 receivers. We use these data, via a straightforward traveltimes inversion, to estimate the velocity structure inside the pyramid.

DATA ANALYSIS

In viewing the raw three-component seismic data, we find that the vertical component shows good quality and consistent first breaks. Some reflections are visible, especially above 150 ms, with different apparent slopes (Figure 2). Channel #5 is dead and channel #1 is noisy. Unfortunately, the H1 component had 6 dead channels out of 10 geophones. The H2 component data has only one dead channel (#2), but it seems the quality is not as high as the vertical component. The right panel of Figure 2 shows the data with a 150 ms window AGC operator.

We pick the first positive peak of every vertical component trace (blue dots on Figure 2 right), and also display the H1 and H2 sections. Due to unreliable or no data, interpolation is applied to pick the first break on channel #5 and #1. These times are listed in Table 2.

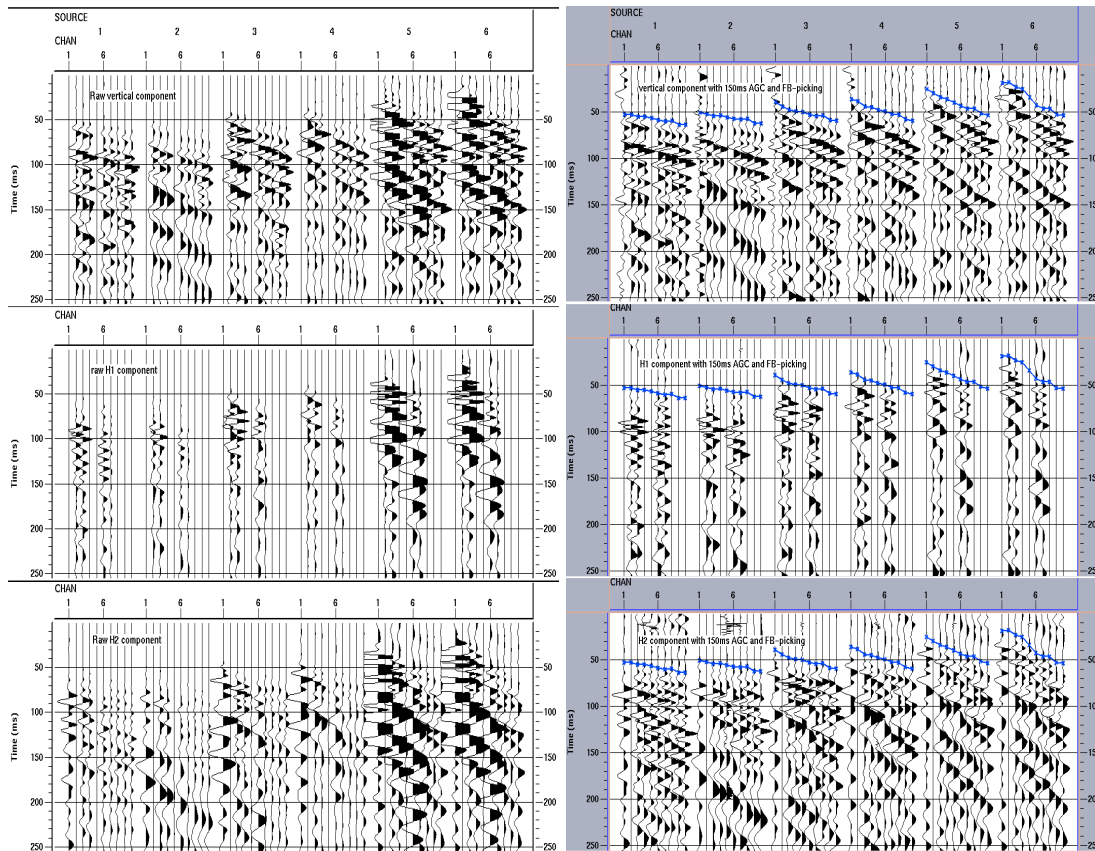


Figure 2. Display of Vertical (V), horizontal-X (H1) and horizontal-Y (H2) components shot gather of raw data (left panel) and after AGC (right panel). The first-break picks are shown on the AGC section.

Table 1. Trace editing of the 3-C geophones.

	Vertical	H1	H2
Dead trace #	5	1, 4, 5, 8, 9, 10	2
Bad trace #	1	None	None

Table 2. The list of first break time picks (ms) from the vertical component data.

	Shot 1	Shot 2	Shot 3	Shot 4	Shot 5	Shot 6
R 1	52.97	47.15	39.43	36.18	27.64	12.03
R 2	52.18	51.59	44.26	38.88	31.38	16.32
R 3	54.76	54.36	47.03	44.26	33.56	23.31
R 4	55.20	53.97	47.36	44.85	36.28	25.73
R 5	56.70	56.06	50.20	47.43	39.90	32.96
R 6	58.53	57.42	52.58	50.01	43.66	43.07
R 7	60.31	58.53	54.17	51.99	46.44	46.64
R 8	59.32	57.93	53.77	52.58	47.03	46.83
R 9	63.88	62.09	58.92	57.53	51.39	52.98
R 10	63.88	62.88	59.91	59.12	53.77	53.97

The hammer-seismic source produces a fairly broadband signal from about 5 Hz to 155Hz. Figure 3 displays the amplitude spectrum of shot #1. The five other shots show similar spectra.

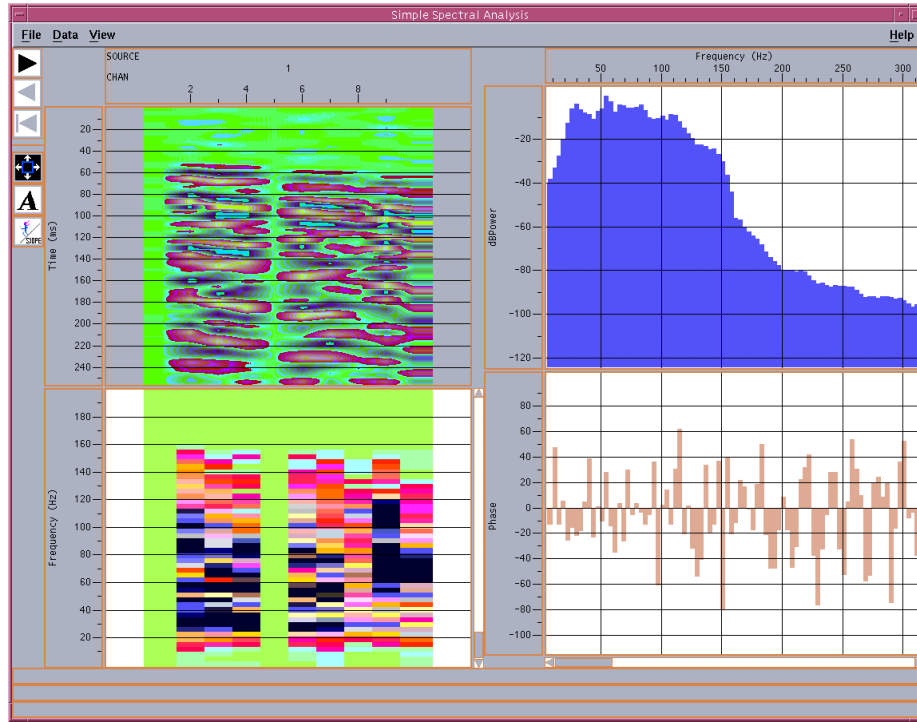


Figure 3. Display of amplitude spectrum for shot #1.

INVERSION AND ANALYSIS

Inversion procedure

We assume straight raypaths and thus cast the tomographic traveltme inversion as a system of 60 linear equations:

$$t_i = \sum_j D_{ij} \cdot s_j \quad (1)$$

where t_i is total traveltme of i^{th} shot-receiver pair, s_j is slowness of j^{th} grid, and D_{ij} is the distance of i^{th} ray traveling in j^{th} grid. Each shot-receiver pair builds one equation.

Expressed in matrix form:

$$t = D \cdot s \quad (2)$$

Defining the grid

First, we need to determine how many bins or pixels there should be. To keep the problem overdetermined, the number should not exceed 60. If we set $dx = dz = 4$ m, there will be 7 rows and 6 columns, or a total of 42 pixels – about half of which will be intersected. So, we use 4 m by 4 m pixels. With same bin size, different origin positions result in different x ranges (-3~21) m distribution if we show a type of grid, which is somewhat different

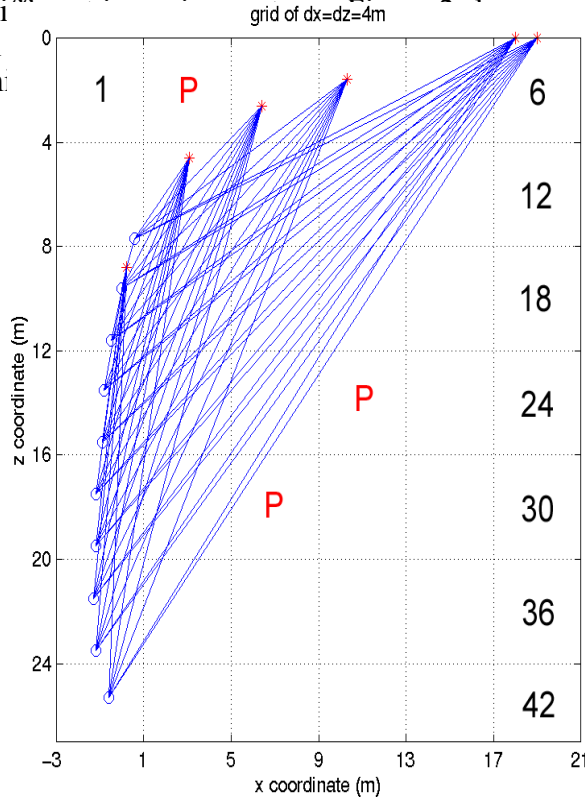


Figure 4. Grid with x range (-3~21) m and bin size $dx=dz=4$ m. Red (*) symbols represent shot points; blue (o) symbols denote receiver points. Bin index numbers are shown on the right.

Calculating matrix **D**

Given the coordinates of the shots and receivers, **D** is calculated. In this case, $dx = dz = 4$, the size of **D** is 60×42 . The matrix **D** is defined when the grid is defined.

To solve the model parameter \mathbf{s}_{inv} (slowness vector), two methods are used: singular value decomposition (SVD) and conjugate-gradient (CG). In SVD, the stabilization factor is $1.0e-6$ in the following computation.

MODEL AND REAL DATA

Noise-free model

Before considering the real data, we start from a constant velocity model to test the algorithm. We set the velocity $v_c = 500$ m/s in every bin, so $s_c = 2$ ms/m. Next the traveltimes \mathbf{t}_{test} are calculated by $\mathbf{D} * \mathbf{s}_c$, then the inversion is undertaken to get \mathbf{s}_{inv} .

We compare the inversion results \mathbf{s}_{inv} with the initial moel values \mathbf{s}_c , and the predicted data $\mathbf{t}_{predict}$ with original data \mathbf{t}_{test} .

The SVD method provides exact results for these noise-free data. After 20 iterations, the conjugate-gradient method had still not converged, but had a residual of $2.51e-05$.

Adding noise

We add random noise to \mathbf{t}_{test} using $RANDN*0.5$ (this random vector has mean zero and variance 0.5). Comparing the value of \mathbf{t}_{test} which range from 7 to 70, the systemic noise level is quite low.

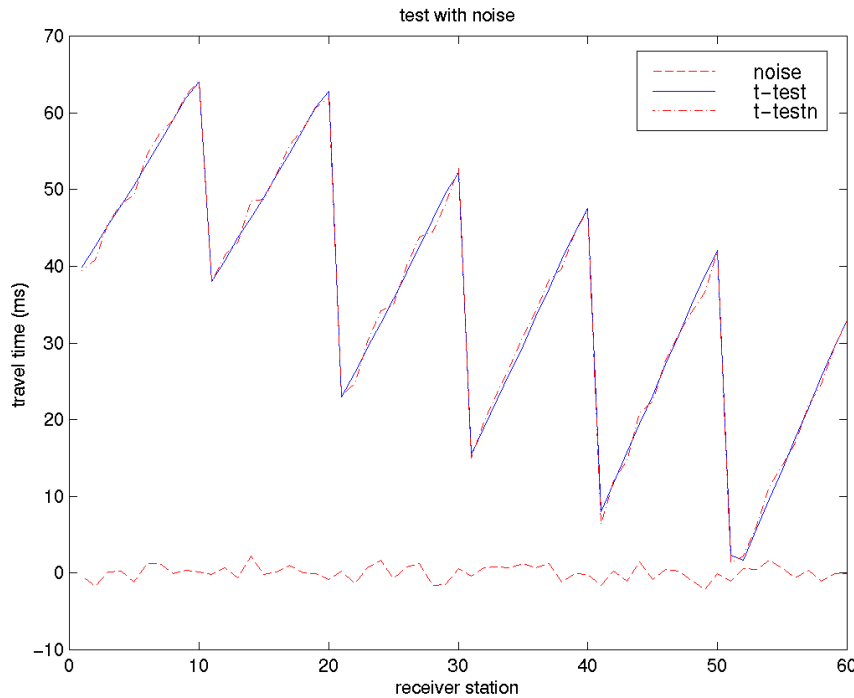


Figure 5. Comparison of noised travelttime from model of slowness = 2ms/m, inverted travel time by SVD method and noise.

The times calculated from the inversion estimates fit the original data very well using the SVD method (Figure 5). The CG method was not as accurate.

Real data:

The \mathbf{t}_{test} is replaced by the first-break times picked from the real data, then we obtained the following result:

Result of Conjugate-gradient method:

flag = 1
 relres = 5.9710e-05
 iter = 20

s_tomo =		v_tomo =	1.00E+03 *								
0	1.8654	2.8750	-0.9216	1.1590	1.4969	0	0.5361	0.3478	0	0.8628	0.668
13.197	4.1034	5.0379	2.6536	2.1589	0	0.0758	0.2437	0.1985	0.3768	0.4632	0
6.1904	1.2759	2.2507	2.4109	0	0	0.1615	0.7838	0.4443	0.4148	0	0
3.8548	2.6031	2.2932	0.9422	0	0	0.2594	0.3842	0.4361	1.0613	0	0
2.3702	1.5228	0.9502	0	0	0	0.4219	0.6567	1.0524	0	0	0
2.2005	2.8322	0	0	0	0	0.4544	0.3531	0	0	0	0
1.9927	0	0	0	0	0	0.5018	0	0	0	0	0

Result of SVD:

s_tomo =		v_tomo =									
0	14.636	2.8557	-0.6943	1.2660	1.4996	0	68.3266	350.1739	0	789.9092	666.6497
12.835	3.9986	4.8449	2.5044	1.7397	0	77.9147	250.0899	206.4042	399.3031	574.8036	0
6.2566	1.4062	2.2625	3.5164	0	0	159.8300	711.1178	441.9879	284.3788	0	0
3.8406	2.6596	1.6463	2.9190	0	0	260.3742	375.9926	607.4177	342.5782	0	0
2.3330	1.4889	-1.1786	0	0	0	428.6312	671.6187	0	0	0	0
2.1841	3.4308	0	0	0	0	457.8452	291.4811	0	0	0	0
2.0046	0	0	0	0	0	498.8464	0	0	0	0	0

There are several negative slowness values that are unphysical. Looking closely, although the CG method is still converging, most of the velocity values of the two methods are close. The final velocity 3-D bar map and contour map are shown in Figure 7.

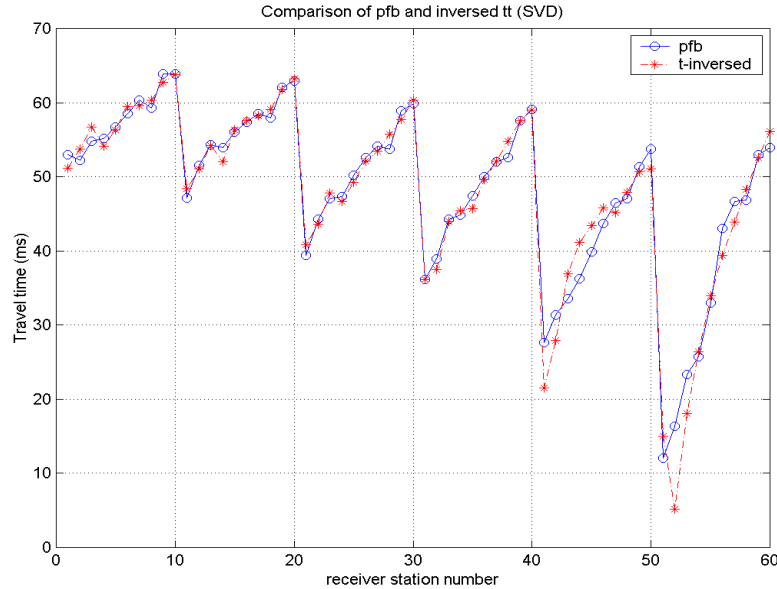


Fig. 6. Comparison of the observed first-break times and calculated times from inversion-estimated slowness model. #52, which has the shortest shot-receiver distance, shows the biggest gap.

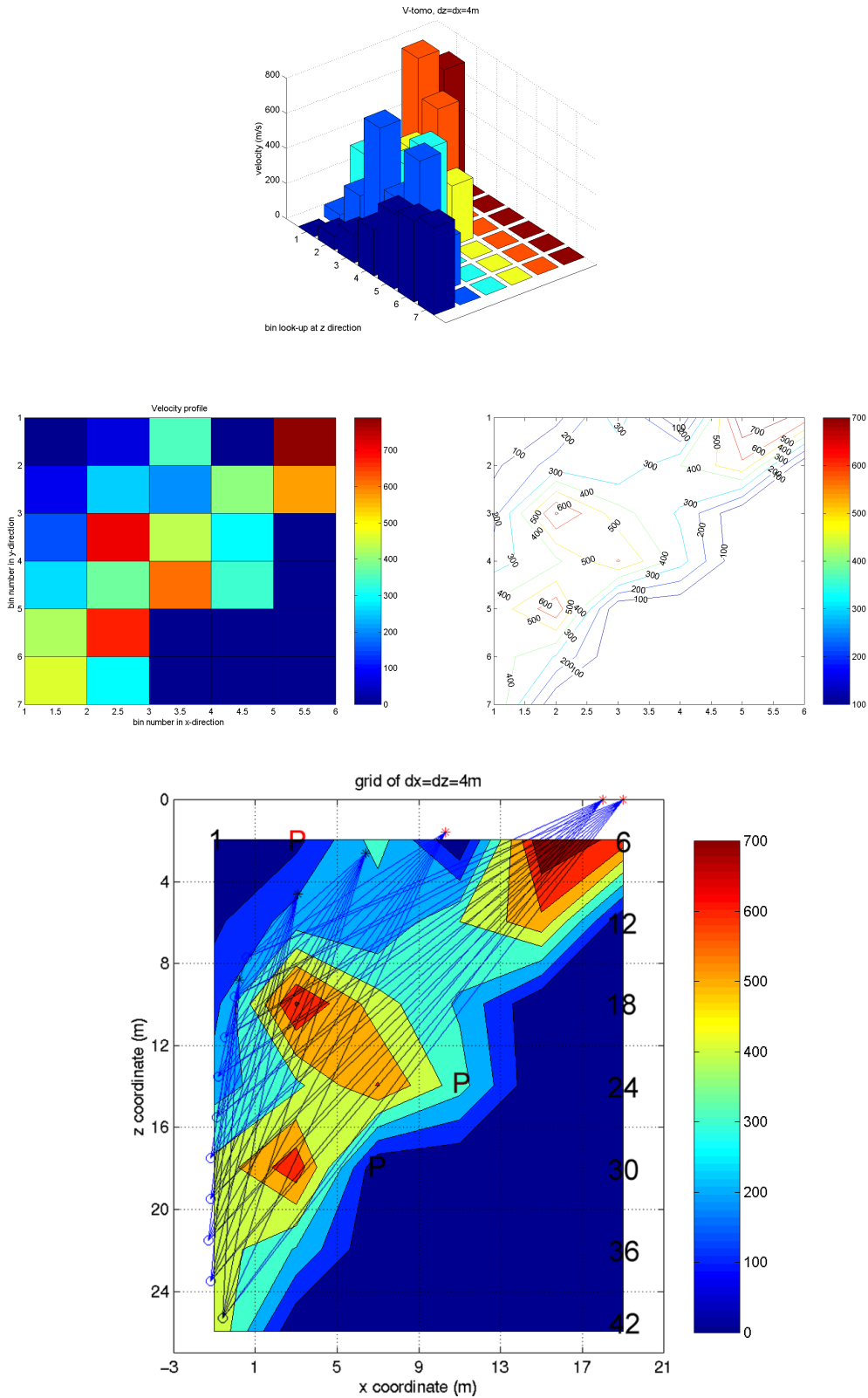


Fig. 7. Displays of the final velocity (m/s) maps calculated by the SVD method. A 3-D view is shown in the top chart. Below the chart are a color map of the velocities and contour map. A full color-contour map with annotated rays is displayed at the bottom of the Figure.

The modeled traveltimes fit the raw data reasonably well. The questions arise: How much can we trust the inversion result? How should we evaluate an inversion system, its resolution, and its error? The solution of the generalized inverse problem is less useful without some description of its uniqueness and reliability.

RESOLUTION AND ERROR ANALYSIS

For the linear equation, $d = Gm$, the exact inverse of $G = U\Lambda V^H$, if it exists, can be written as $G^{-1} = V\Lambda^{-1}U^H$, where “H” indicates Hermitian transpose which means $A^H = (A^*)^T = (A^T)^*$. Aki and Richards (1980) consider the so-called *generalized inverse operator*

$$G_g^{-1} = V_p \Lambda_p U_p^H \quad (3)$$

as an inverse operator to the operator

$$G = U_p \Lambda_p V_p^H \quad (4)$$

U is composed of U_p and U_0 , where U_p consists of the eigenvectors with nonzero eigenvalues and U_0 consists of the eigenvectors with zero eigenvalues. The same holds with V , V_p and V_0 . U_0 -space is the source of discrepancy between the observed data and the prediction by operator G . On the other hand, V_0 -space is the source of non-uniqueness in determining the model from the data.

Because of orthogonality, $U_p^H U_p = V_p^H V_p = I$, but when U_p and V_p are no longer complete, $U_p U_p^H \neq I$, $V_p V_p^H \neq I$, U_p and V_p are coupled through the nonzero eigenvalues.

The resolution in model space is

$$m_g = V_p \Lambda_p U_p^H U_p \Lambda_p V_p^H m = V_p V_p^H m \quad (5)$$

The resolution in data space is:

$$d_g = G G_g^{-1} d = U_p U_p^H d \quad (6)$$

The reliability of the solution is measured by its covariance matrix.

$$\langle \Delta m_g \Delta m_g \rangle = \sigma_d^2 G_g^{-1} G_g^{-1} = \sigma_d^2 V_p \Lambda_p^{-2} V_p \quad (7)$$

The singular value decomposition of matrix D is performed in Matlab. There are 42 model parameters in 60 equations, the size of D is 60×42. So, U is 60×42, Λ is 42×42 and V is 42×42. In the eigenvalue matrix Λ (shown in Figure 8), the first 24 diagonal elements are non-zero, 25~32 are very small numbers which range from level of 10^{-16} to 10^{-32} , which are believed to be the computation errors due to machine resolution. Therefore, the number of non-zero eigenvalue (p) of this particular linear equation problem is 24, less than the number of model parameters, which tell us both V_0 and U_0 space exist.

In this case, \mathbf{V}_p and \mathbf{U}_p is the matrix formed by the first 24 columns of \mathbf{V} and \mathbf{U} , respectively. So, \mathbf{V}_p is 42×24 , \mathbf{U}_p is 60×24 . Λ_p , matrix of 24×24 , is the left upper part of Λ .

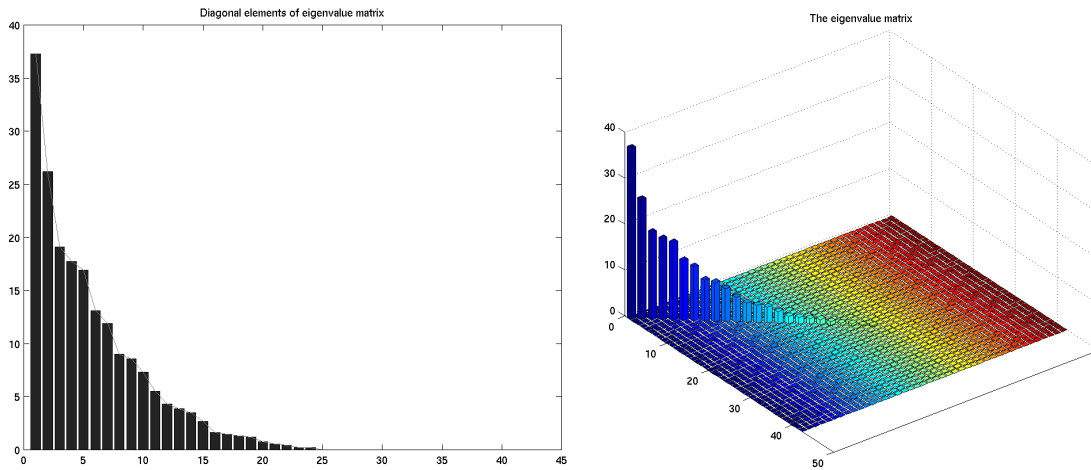


Fig. 8. 3D display of the eigenvalue matrix Λ (right) and 2D display of its diagonal elements (left).

Now, we calculate the resolution matrix in model space. Based on equation (5), the resolution matrix $\mathbf{V}_p \mathbf{V}_p^H$ is shown in Figure 9. It is observed that the diagonal elements are only two values: 1 and 0. Back to Figure 2, the 42 model parameters correspond to the 42 bins. The bin with diagonal element value of 0 in the resolution matrix is the one that has no raypaths in it. The resolution matrix successfully separates the model parameters into two groups, with contribution to data (corresponding to non-zero eigenvalues) and without contribution to data (corresponding to zero eigenvalues). Through this figure, we know that there are 24 model parameters that can be solved and which bins they are. However, what we don't know is how much we can trust the solved 24 parameters.

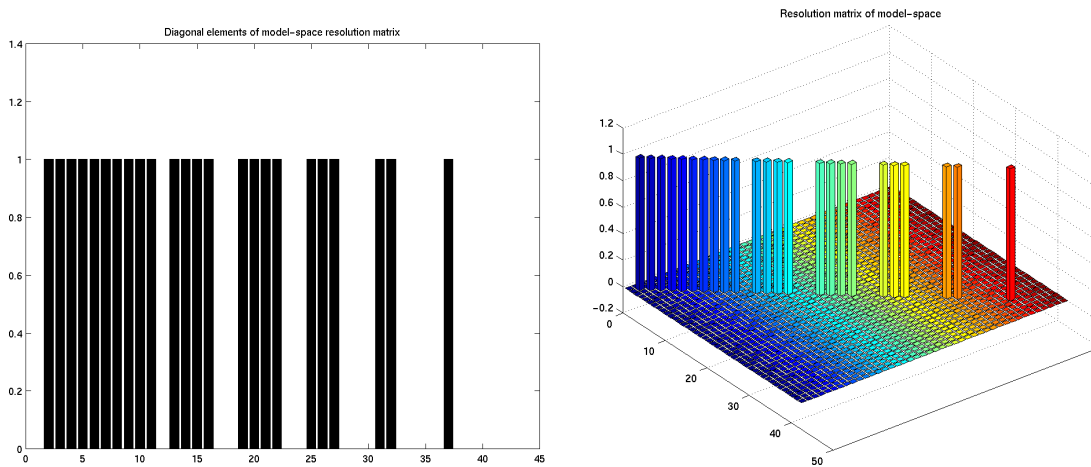


Fig. 9. 3D display of the model space resolution matrix $\mathbf{V}_p \mathbf{V}_p^H$ (right) and 2D display of its diagonal elements (left).

The next step is to compute the resolution matrix $\mathbf{U}_p \mathbf{U}_p^H$ in data space, which point to the discrepancy between the observed and predicted data. It is more complex than the model space resolution matrix (Figure 10). In the 60 diagonal elements, the observed trend is that the data with longer travel distance usually have higher covariance level, i.e., the tenth receiver is nearly highest in each shot group. Notice the lowest value is at trace 52, the pair of 6th shot and 2nd receiver, which has the shortest distance. The higher, the better.

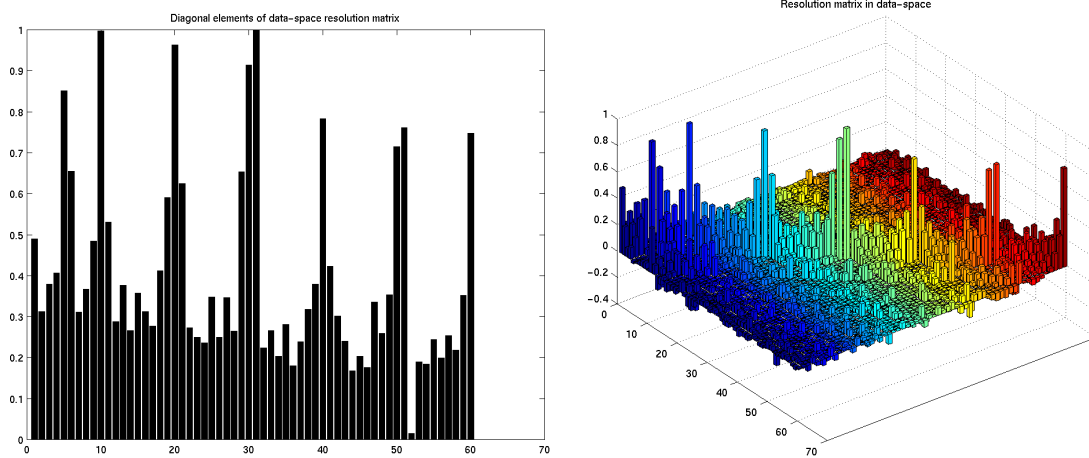


Fig. 10. 3D display of the data space resolution matrix $\mathbf{U}_p \mathbf{U}_p^H$ (right) and 2D display of its diagonal elements (left).

Finally, we should calculate the covariance of the solution. The error of model space is associated with the error of the data space. What we calculate is the weights matrix of data variance in equation (7) based on the assumption of data have same σ_d^2 . This weighting factor is like an amplifier. So, the lower, the better (Figure 11). We set a certain value as the acceptable reliability level, model parameters higher than this level are thought to be unreliable, and those lower are reliable. In this example, if we set 6.5 as the threshold value, the weights in bin #2, #22, #27 are higher than 6.5, which indicates the inversed slowness in these three bins are not reliable. Looking back at Figure 2, the bins marked with 'P' are those three. We see only 1~3 raypaths go through these bins and there are no crossing points, that's the reason they have lower reliability.

What about the effect of Marquardt factor, or stable factor ϵ to the resolution? It will change the absolute value of the elements in the resolution matrix. The bigger the ϵ is, the lower the weight. The function of ϵ is to smooth the model error, make it more reliable. However, the relative position of each diagonal element is fixed. In other words, if we draw a line to connect the value of diagonal elements of the resolution weights matrix, the shape of this curve will keep similar whatever ϵ is. When we choose a suitable threshold, the same 3 bins are still above the level.

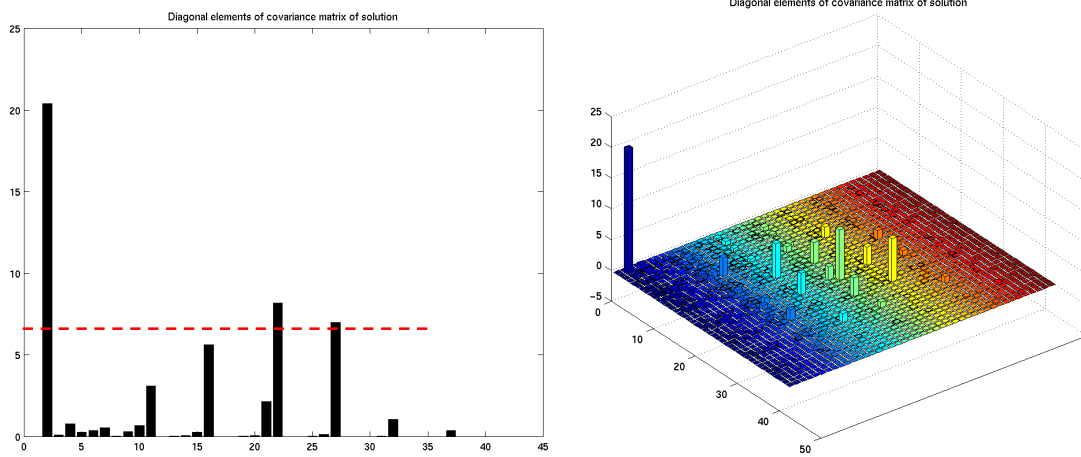


Fig. 11. 3D display of the reliability matrix $\mathbf{U}_p \mathbf{U}_p^H$ (right) and 2D display of its diagonal elements (left).

DISCUSSION

The resolution of model space and data space are calculated through the non-zero eigenvectors of \mathbf{v}_i and \mathbf{u}_i , $i = 1, \dots, p$.

The conjugate-gradient method starts from setting all the model parameters to 0. Slow or non-convergence can happen whenever the initial estimate of the model is poor (Lines and Treitel, 1984). This may be the reason that the CG method is not convergent after 20 iterations in our case.

Based on the assumption of straight-line raypath and the fact that one non-zero eigenvalue corresponds to one bin which does contain a part of the raypath, we can find all the bins with contribution to data when the grid origin, grid size and the locations of shots and receivers are defined. Those bins that don't contain raypaths correspond to the zero-eigenvalues, and should be kept out of the computation.

If we only keep the non-zero eigenvalues in $\mathbf{\Lambda}$, or $\mathbf{\Lambda}_p$, the $\mathbf{\Lambda}_p^{-1}$ will always exist. For small inversion problem, like this case, we can just use \mathbf{V}_p , \mathbf{U}_p and $\mathbf{\Lambda}_p$ to get the inversion result. But when the number of model parameters increases, to several thousand say, the exact analytic method becomes very time-consuming. Then the conjugate-gradient method will show an advantage over the SVD method.

The above discussion is based on the grid bd: How should it be defined? What is an optimal grid? Can we determine this by some sort of mathematical expression? Because the source offset of this VSP-like geometry is limited, the coverage angle is not wide enough to detect the center of the pyramid, a further full-angle tomographic survey (cross-well VSP style) is recommended.

CONCLUSIONS

A seismic tomographic data set of traveltimes from around a Maya pyramid is analyzed. Using singular value decomposition we solve for velocity structure in an inversion based on the straight raypaths.

The inversion result is made more complete with uniqueness, resolution and reliability analysis. The velocity profile shows that at the surface velocity is about 100~200 m/s, and the inner part has higher velocity about 500 m/s, even 700 m/s somewhere. There is a lower velocity area between the two high velocity peaks.

ACKNOWLEDGEMENTS

We are grateful to the Chan Chich Lodge, Belize for allowing collection of these data. In particular, Dr. B. Houk, archeologist at the Chan Chich site and Dr. Jaime Ava of the Department of Archeology, Government of Belize. Dr. Fred Valdez, Jr. University of Texas at Austin and Dr. Leslie Shaw of Bowdoin College, Maine provided much-appreciated field support. Dr. Claire Allum, Mr. Adam Jagihch, and Ms. Stacie Stasko ably assisted in data acquisition. Mssrs. Eric Gallant and Henry Bland of the CREWES Project, University of Calgary kindly assisted with the seismic equipment, logistics, and data handling.

REFERENCES

- Aki, K. and Richards, P., 1980, Quantitative Seismology – Theory and Methods: W.H. Freeman Co., vol. 2.
- Lines, L.R. and Treitel, S., 1984, Tutorial: A review of least-squares inversion and its application to geophysical problems, *Geophysical Prospecting* 32, 159-186.